Nonlinear Dyn (2012) 67:965–985
DOI 10.1007/s11071-011-0040-4

ORIGINAL PAPER

Dynamic modeling and wind vibration control of the feed support system in FAST

Zhu-Feng Shao · Xiaoqiang Tang · Li-Ping Wang · Xu Chen

Received: 7 June 2010 / Accepted: 30 March 2011 / Published online: 27 April 2011

Abstract The Feed Support System (FSS) addressed here is the receiver carrier of the Five-hundred-meter Aperture Spherical radio Telescope (FAST) in China. The FSS is a complex hybrid manipulator, which consists of a cable-driven Stewart manipulator, an A–B rotator and a rigid Stewart manipulator. The cable-driven Stewart manipulator, which is a long-span flexible cable structure, is sensitive to the wind disturbance and induces the FSS vibration. The rigid Stewart manipulator is designed to suppress the vibration and improve the terminal accuracy of the FSS. In the paper, the elastic dynamic model of the cable-driven Stewart manipulator is deduced by simplifying the flexible cable as the spring damping model, while the rigid-body dynamic model of the A–B rotator and the rigid Stewart manipulator is obtained in detail, using the Newton–Euler method. The internal coupling forces of the FSS are figured out. The wind disturbance model is established according to the Davenport spectrum. By adopting the kinematic and dynamic parameters of the FAST prototype, the simulation model of the FSS is completed. Kinematic and dynamic vibration control strategies are evaluated with simulations. Results show that the dynamic vibration suppression strategy well satisfies the FSS terminal accuracy requirement, keeps the rigid Stewart manipulator working with reasonable driving forces, and should be adopted in the control system of the FAST prototype.

Keywords Vibration control · Wind disturbance · Newton–Euler method · Dynamic equation · Parallel manipulator

Z.-F. Shao · X. Tang (✉) · L.-P. Wang · X. Chen
Institute of Manufacturing Engineering,
Department of Precision Instruments and Mechanology,
Tsinghua University, Beijing 100084, China
e-mail: tang-xq@mail.tsinghua.edu.cn

1 Introduction

The Large Telescope (LT), also known as the square kilometer array, was first proposed at the General Assembly of the International Union of Radio Science (URSI) in 1993. In 1994, Chinese astronomers carried out the conceptual design of the Five-hundred-meter Aperture Spherical radio Telescope (FAST), which will be located in the Karst region of Guizhou Province, southwestern China. With the joint efforts of Chinese astronomers and engineers, the layout design of the FAST has already been accomplished [1, 2].

A typical radio telescope is composed of a reflector and a receiver. However, due to the large aperture, the mechanical structure of the FAST, as shown in Fig. 1, has two outstanding features:

(1) The active main reflector. The 520-m-diameter reflector, divided into 2000 small elements, can correct spherical aberration to achieve the full polarization and a wide reflecting band.

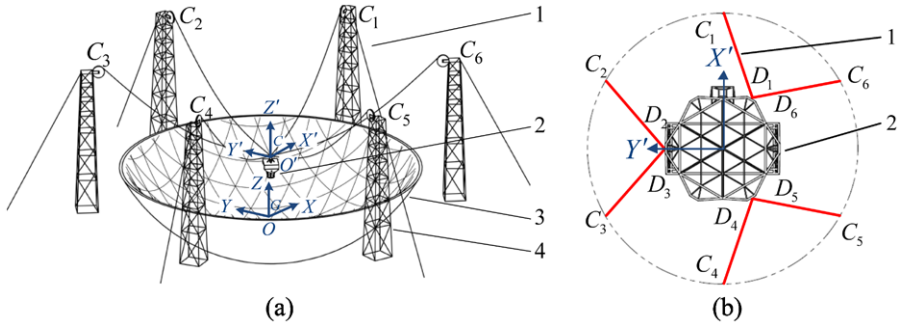

Fig. 1 The sketch map of the FAST: (**a**) Isometric view. (**b**) Top view. 1: cable-driven Stewart manipulator (the base is defined by six cable-tower connection points C_1, C_2, C_3, C_4, c_5 and C_6), 2: feed cabin, 3: active main reflector (520-m diameter), 4: towers (uniformly distributed in a 600-m-diameter circle)

(2) The Feed Support System (FSS). The complex hybrid system consists of three parts: a cable-driven Stewart manipulator, an A–B rotator and a rigid Stewart manipulator. The A–B rotator and the rigid Stewart manipulator are mounted in the feed cabin, as shown in Fig. 2. The rigid Stewart manipulator is usually called the Secondary Adjustable System (SAS), while the end effector of the cable-driven Stewart manipulator is usually called the cable platform, for short. The terminal receivers of the FAST are attached to the SAS end effector (FSS terminal).

These three parts are arranged in series. The A–B rotator is the intermediary which connects the cable platform and the SAS base at either end. In mechanical structure, the A–B rotator can be considered as being composed of the cable platform, the SAS base and the framework, as shown in Fig. 2. As the range of observation angle for the FAST is from 40° to −40°, which is far beyond the rotation capacity of the cable-driven Stewart manipulator, the A–B rotator is designed to release the rotation burden of the cable-driven Stewart manipulator.

The FSS is a typical macro/micro manipulator system, which is usually composed of a large (macro) robot carrying a small (micro) high-precision robot such as a parallel manipulator. The small high-performance manipulator answers for local operation, while the system retains the high speed and large work space of the large robot [3]. In FAST, the cable-driven Stewart manipulator and the A–B rotator, which constitute the hybrid macro robot, provide the FSS terminal with a wide range of translation and rotation. However, the

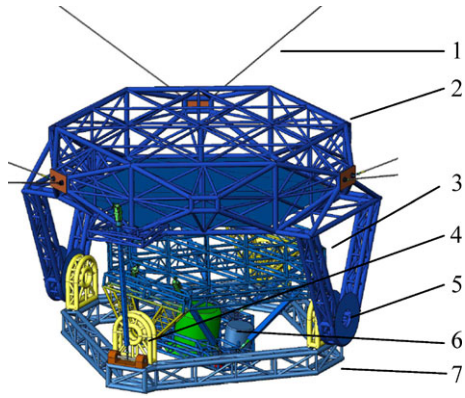

Fig. 2 The sketch map of the feed cabin. 1: cables, 2: end effector of the cable-driven Stewart manipulator (cable platform), 3: rigid Stewart manipulator (SAS), 4: A-axis of the A–B rotator, 5: B-axis of the A–B rotator, 6: receivers, 7: framework

cable-driven Stewart manipulator is a long-span flexible cable structure vulnerable to vibration. The SAS is responsible for reducing the vibration of the FSS terminal and improving the terminal trajectory accuracy of the FSS, to achieve the terminal pointing accuracy of 8′ and positioning accuracy of 10-mm in RMS (root mean square). According to such function classification, the cable-driven Stewart manipulator and A–B rotator (macro robot) are controlled at low frequency to track the astronomical observation trajectory. The SAS is controlled at high frequency to restrict the system vibration resulting from the wind disturbance and reduce the FSS terminal error. Obviously, the SAS vibration control strategy is the kernel of the FSS control system.

As shown in Fig. 3, the SAS is a 6-degrees-of-freedom (6-DOF) parallel manipulator [4], with two

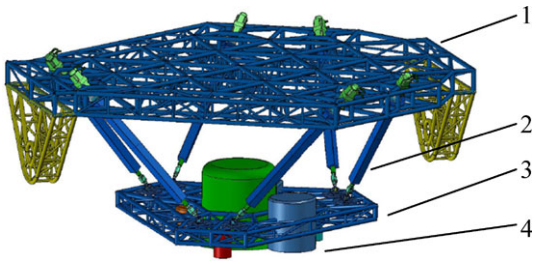

Fig. 3 The sketch map of the SAS. 1: base, 2: extensible limbs, 3: end effector, 4: receivers

bodies (the end effector and the base) connected together by six extensible limbs. Each limb, driven by a servomotor and lead screw, is connected with the base by a universal joint at one end and the end effector by a spherical joint at the other. For the cable-driven Stewart manipulator, the end effector is connected to the base by six cables, as shown in Fig. 1. Each cable is driven by a servo mechanism, which is composed of a winch, a reducer, and a servomotor [5].

The vibration of the FSS will affect the overall observing performance of the FAST. The vibration analysis and control are inevitable to accomplish the FAST project. In order to establish the simulation model, the dynamic model of the FSS needs to be deduced at first. However, due to the complex and coupled mechanical structure, the dynamic model of the FSS is inherently difficult. The dynamic model of the FSS can be subdivided into the elastic dynamic model of the cable-driven Stewart manipulator, as well as the rigid body dynamic model of the A–B rotator and the SAS. Based on different mechanics principles, several methods can be adopted to establish the dynamic model, such as the Newton–Euler method [6–9], the Lagrangian formulation [10–12], the principle of virtual work [13–16], and the Kane method [17, 18]. However, the Newton–Euler formulation, recognized as the approach with clear physical meaning and good suitability for the complex structure modeling, is adopted in this article.

The remainder of this paper is organized as follows. In the next section, the structure of the FSS studied here is described in detail. The wind disturbance model is established on the basis of the Davenport spectrum [19] in Sect. 3. The elastic dynamic model of the cable-driven Stewart manipulator and the numerical solution are demonstrated in Sect. 4. The dynamic model of the A–B rotator and the SAS is obtained in algebraic form in Sect. 5. The vibration frequency and stiffness of the FSS are analyzed in Sect. 6. In Sect. 7, the wind vibration simulation of the FSS is carried out. To improve the terminal accuracy, the vibration control simulations are carried out in Sect. 8. Finally, conclusions of this paper are given in Sect. 9.

2 System description

As shown in Fig. 1, the base of the cable-driven Stewart manipulator is defined by six cable-tower connection points (C_1, C_2, C_3, C_4, C_5 and C_6). The global frame $\{\boldsymbol{G}\}$ is an inertia coordinate system O–XYZ, attached to the bottom of the active main reflector with X-axis pointing to the bottom of tower C_1, and Y-axis crossing the midpoint of C_2 and C_3 tower bottoms. The cable frame $\{\boldsymbol{C}\}$ is attached to the geometric center defined by the end-effector points of the cable-driven Stewart manipulator, as shown in Figs. 1 and 4. Let $\{\boldsymbol{P}\}$ be the SAS end-effector frame o–xyz, attached to the geometric center of the SAS end effector plane determined by SAS end-effector points with the x-axis crossing the midpoint of P_1P_6, and the z-axis perpendicular to the SAS end-effector plane. Let $\{\boldsymbol{B}\}$ be the SAS base frame o'–$x'y'x'$, attached to the geometric center of the SAS base plane defined by the SAS base points, with the x'-axis crossing the midpoint of B_1B_6, and the z'-axis perpendicular to the SAS base plane. The middle frame $\{\boldsymbol{M}\}$ is a translational coordinate, attached to the intersection of the two revolution axes in the A–B rotator, parallel to the global frame.

At the initial state of the FSS, the cable platform is at the center of its workspace and driving cables are of uniform length. The FSS terminal is at the center of the SAS workspace, and extensible limbs are of uniform length. The initial distance of the SAS between the base and the end effector is 3.3 m, the initial height of the cable-driven Stewart manipulator is 150.3 m in global frame, and the initial distance between FSS terminal and the cable platform is 10.3 m. Initial rotation angles of the A–B rotator are zero, with $\underline{X}$-axis and $\underline{Y}$-axis in $\{\boldsymbol{M}\}$ along A-axis and B-axis of the A–B rotator, respectively. At the initial state, these five frames are parallel to each other with the Z'-axis, the Z-axis, the $\underline{Z}$-axis, the z-axis, and the z'-axis collinear, along the opposite direction of the gravity.

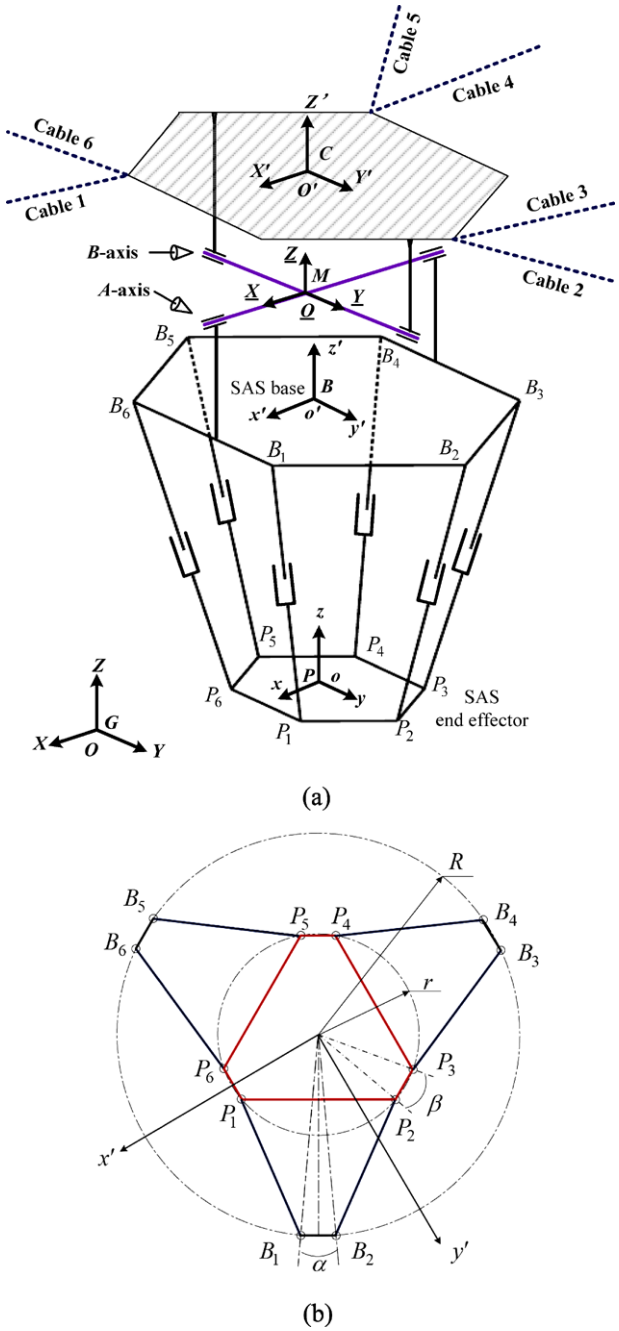

Fig. 4 Kinematic model of the FSS: (**a**) isometric drawing of the FSS, (**b**) top view of the SAS

Some important notations used in this paper are shown in Table 1. Others have been described at the place of first appearance. Generally, vectors and matrices are described in bold. The SAS limb number is denoted by the subscript i ($i = 1, 2, \ldots, 6$), while the cable number is denoted by the subscript j ($j = 1, 2, \ldots, 6$). The right subscripts of notations hint at their physical meanings, while the left superscripts show the coordinate systems under which they are described.

3 Wind disturbance model

In this section, the wind impact, the major external disturbance for the FSS, is represented as uniformly distributed force acting on the feed cabin shield, which

Table 1 Notation description

Symbol	Physical meaning	In frame
${}^{G}\mathbf{R}_{C}$	Rotation matrix. Orientation of the cable platform	Global
${}^{G}\mathbf{t}_{C}$	Translation vector. Position of the cable platform	Global
$\mathbf{d}_j$	Translation vector. Position of the end-effector points of the cable-driven Stewart	Cable
$\mathbf{c}_j$	Translation vector. Position of the base points of the cable-driven Stewart	Global
${}^{C}\mathbf{t}_{M}$	Translation vector. Position of the intersection of revolution axes of the A–B rotator	Cable
${}^{C}\mathbf{R}_{f}$	Rotation matrix. Orientation of the framework	Cable
${}^{C}\mathbf{R}_{B}$	Rotation matrix. Orientation of the SAS base	Cable
$\mathbf{b}_i$	Translation vector. The SAS base points	SAS base
$\mathbf{p}_i$	Translation vector. The SAS end-effector points	SAS end effector
${}^{B}\mathbf{R}_{P}$	Rotation matrix. Orientation of the SAS end effector	SAS base
${}^{B}\mathbf{t}_{P}$	Translation vector. Position of the SAS end effector	SAS base
${}^{B}\boldsymbol{\omega}_{P}$	Angular velocity of the SAS end effector	SAS base
${}^{B}\boldsymbol{\varepsilon}_{P}$	Angular acceleration of the SAS end effector	SAS base

covers the feed cabin. The wind force is determined by the wind velocity. According to the standard theory of Davenport [18], the total wind velocity is the combination of a steady-state (or mean) velocity and a turbulence (or gust) velocity, which can be expressed as a function of height z and time t:

$$v(z,t) = v_m(z) + v_g(z,t), \tag{1}$$

where $v_m(z)$ stands for the mean velocity, and $v_g(z,t)$ stands for the gust velocity.

3.1 Steady-state wind velocity

In normal terrain, the wind velocity increases with the height. The exponential function used to describe the relation between the steady-state wind speed and height can be expressed as

$$v_m(z) = v_{10} \cdot \left(\frac{z}{10}\right)^{\alpha}, \tag{2}$$

where z is the height of the feed cabin center from the ground ($z = 145$ m in our case), v_{10} is the mean velocity measured at 10 m above the ground, and α is the terrain factor reflecting the roughness of the ground surface. According to the physical environment of the FAST site, $\alpha = 0.16$.

The FAST is designed to be operational until the steady-state velocity measured at 10 m height exceeds 4 ms^{-1}, and to be survival until the steady-state velocity exceeds 8 ms^{-1} [2]. According to the exponential function, the steady-state wind speeds of different height are calculated. As shown in Fig. 5, the maximum operational mean speed is 6.136 ms^{-1} at feed-cabin height (145 m) and the survival mean speed is 12.27 ms^{-1} at feed-cabin height.

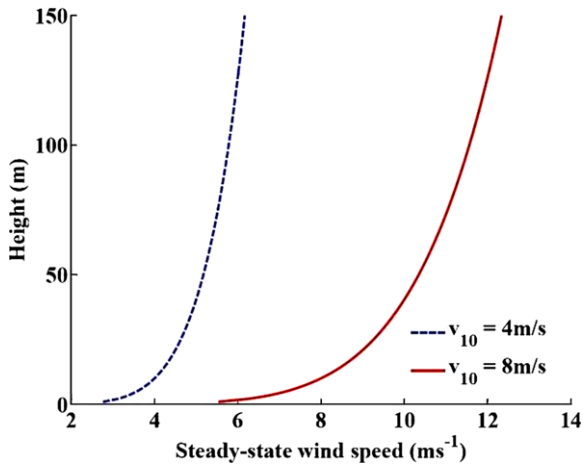

Fig. 5 Steady-state wind speed

3.2 Turbulence wind velocity

The gust component, which is a stationary Gaussian random process with zero mean, is usually analyzed with the random vibration theory. Davenport has made a large number of wind tunnel tests and gave a widely

used wind spectrum, which depends on the mean wind velocity and the terrain roughness. The Davenport spectrum [18] can be expressed as

$$S_v(f) = \frac{4\kappa v_m^2 \beta}{f(1+\beta^2)^{4/3}}, \tag{3}$$

where $\beta = L_v f / v_m$, L_v is the wind turbulence scale, f is the gust frequency, and κ is the surface drag coefficient ($0.005 \le \kappa \le 0.015$). For the FAST project, $L_v = 1200$ m and $\kappa = 0.01$.

The gust velocity can be obtained by inputting a white-noise signal of unit standard deviation into the approximation filter of the Davenport spectrum. The filter transfer function adopted here is of the third order, which is obtained by adjusting parameters until the filter consistent with the Davenport spectrum is well within the bandwidth of $[10^{-4}, 10]$ Hz.

Finally, the approximation filter is selected, whose transfer function can be described as

$$TF = \frac{1.869s^2 + 1.147s + 0.002927}{s^3 + 1.646s^2 + 0.1057s + 0.0008963}. \tag{4}$$

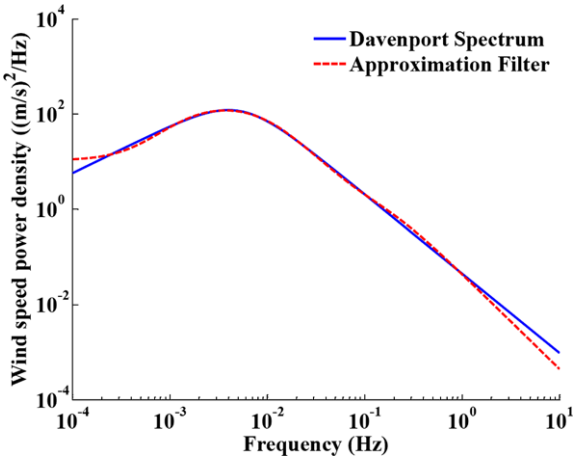

Fig. 6 Comparison between the Davenport spectrum and the approximation filter

The comparison of the filter and the Davenport spectrum is shown in Fig. 6. As demonstrated in the figure, the filter approximates the Davenport spectrum well. Besides, the main wind effect occurs around 0.01 Hz, which can be compensated by the feed support system in FSS.

3.3 Wind force

On the basis of wind velocity, the time history of the wind force is obtained in this section. Firstly, the wind pressure exerted on the feed cabin shield is calculated. According to the Bernoulli Equation, the wind pressure can be expressed as

$$p(z,t) = \frac{1}{2}\rho v(z,t)^2 = \frac{1}{2}\rho\left[v_m(z) + v_g(z,t)\right]^2, \tag{5}$$

where ρ is the air density, and $\rho = 1.225\ \mathrm{kg\,m^{-3}}$ in the FAST site.

The wind force acting on the FSS is the product of wind pressure and effective area. The effective area of the feed cabin shield under wind pressure is 150 m^2. The simulation procedure of the wind force in FAST is given in Fig. 7. Further, a sample of the FSS wind force generated with the method is shown in Fig. 8, which is used in the following simulations.

4 Elastic dynamic model of the cable-driven Stewart manipulator

In order to simplify the dynamic model of the cable-driven Stewart manipulator, each driving cable is considered as the spring damping model. The elastic model of the cable-driven Stewart manipulator is shown in Fig. 9.

The jth cable vector ${}^G\mathbf{S}_{Cj}$ (from point C_j to point D_j) can be derived under the global frame as

$${}^G\mathbf{S}_{Cj} = {}^G\mathbf{t}_C + {}^G\mathbf{R}_C \cdot \mathbf{d}_j - \mathbf{c}_j. \tag{6}$$

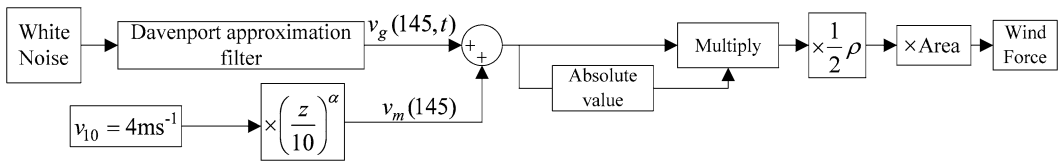

Fig. 7 Wind force calculation flow chart

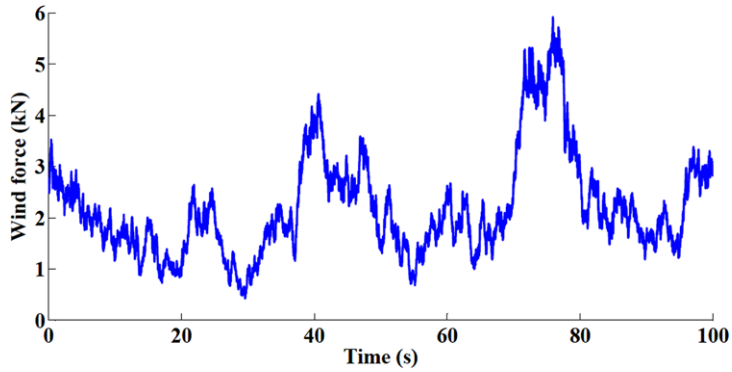

Fig. 8 A sample of the FSS wind force

Since the mass of the feed cabin is over 30 ton and the cable mass is less than 1 ton, it is reasonable to neglect the mass of each driving cable. Then the cable can be considered as a straight line, and the length of the jth cable can be given as

$$L_{Cj} = \left\| {}^{G}\mathbf{S}_{Cj} \right\|. \tag{7}$$

The unit cable vector can be described as

$${}^{G}\mathbf{s}_{Cj} = {}^{G}\mathbf{S}_{Cj}/L_{Cj}. \tag{8}$$

The velocity of point D_j can be obtained by taking the derivative of the cable vector equation, and is given in terms of the cable platform velocities as

$${}^{G}\dot{\mathbf{S}}_{Cj} = {}^{G}\dot{\mathbf{t}}_{C} + {}^{G}\dot{\boldsymbol{\theta}}_{C} \times \left({}^{C}\mathbf{R}_{C} \cdot \mathbf{d}_{j}\right). \tag{9}$$

The velocity along the driving cable is given by the component of the velocity along the cable vector:

$$\dot{L}_{Cj} = {}^{G}\mathbf{s}_{Cj} \cdot {}^{G}\dot{\mathbf{S}}_{Cj}. \tag{10}$$

The force acting on the cable platform by the jth cable can be calculated in terms of the cable elastic deformation and velocity as

$$F_j = K_j \cdot (L_{Cj} - L_{Cj0}) + \zeta_j \cdot \dot{L}_{Cj}, \tag{11}$$

where K_j is the elastic coefficient of the jth cable ($K_j = \mathrm{A} \cdot \mathrm{E}/L_{Cj0}$, the cable cross-sectional area $\mathrm{A} = 8.04 \times 10^{-4}$ m^2, the cable elastic modulus $\mathrm{E} = 1.6 \times 10^{11}$ Pa), the damping coefficient $\zeta_j = 200$ N s/m, and L_{Cj0} is the theoretical length of the jth cable calculated without external disturbances. According to the Newton–Euler equation, the dynamic equation of the cable-driven Stewart manipulator can be written as

$$\begin{bmatrix} \sum_{j=1}^{6} F_j {}^{G}\mathbf{s}_{Cj} \\ \sum_{j=1}^{6} F_j [({}^{G}\mathbf{R}_{C} \cdot \mathbf{d}_{j}) \times {}^{G}\mathbf{s}_{Cj}] \end{bmatrix}$$

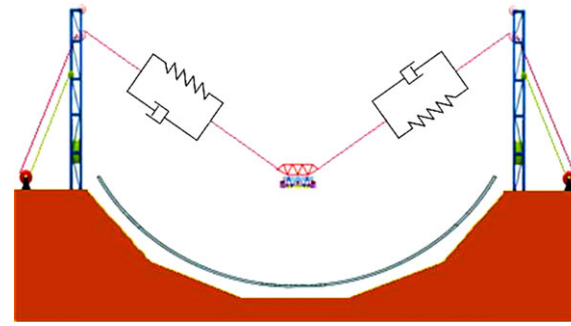

Fig. 9 Elastic model of the cable-driven Stewart manipulator

$$+ \begin{bmatrix} M {}^{G}\ddot{\mathbf{t}}_{C} \\ {}^{G}\dot{\boldsymbol{\theta}}_{C} \times \mathbf{I}\, {}^{G}\dot{\boldsymbol{\theta}}_{C} + \mathbf{I}\, {}^{G}\ddot{\boldsymbol{\theta}}_{C} + M\mathbf{e}_{C} \times {}^{G}\ddot{\mathbf{t}}_{C} \end{bmatrix} = \begin{bmatrix} \mathbf{F}_{e} \\ \mathbf{N}_{e} \end{bmatrix},$$

where M and $\mathbf{I}$ are the mass and inertia matrices of the feed cabin, $\mathbf{F}_e$ and $\mathbf{N}_e$ are the external force and torque acting on the feed cabin, ${}^{G}\ddot{\mathbf{t}}_{C}$ and ${}^{G}\ddot{\boldsymbol{\theta}}_{C}$ are the linear and angular accelerations of the cable platform in global frame, $\mathbf{e}_C$ is the position vector of the mass center of the cable platform in $\{\boldsymbol{C}\}$.

As the algebraic solution of the above dynamic equation is difficult to obtain, fourth-order Runge–Kutta method is adopted to get the numerical solution. Assuming $\mathbf{X} = [{}^{G}\mathbf{t}_{C}; {}^{G}\boldsymbol{\theta}_{C}]$, the elastic dynamic equation of the cable-driven Stewart manipulator can be rewritten as

$$\begin{cases} \dot{\mathbf{X}} = \mathbf{V}, \\ \dot{\mathbf{V}} = f(t, \mathbf{X}, \mathbf{V}), \\ \mathbf{X}(t_0) = \mathbf{X}_0, \\ \mathbf{V}(t_0) = \dot{\mathbf{X}}_0. \end{cases} \tag{12}$$

And the recurrence formulas of the Runge–Kutta method can be deduced as

$$\begin{cases}\mathbf{X}_{n+1}=\mathbf{X}_n+h\mathbf{V}_n+\frac{h^2}{6}(\boldsymbol{\eta}_1+\boldsymbol{\eta}_2+\boldsymbol{\eta}_3),\\ \mathbf{V}_{n+1}=\mathbf{V}_n+\frac{h}{6}(\boldsymbol{\eta}_1+2\boldsymbol{\eta}_2+2\boldsymbol{\eta}_3+\boldsymbol{\eta}_4),\end{cases}$$

where h is the time step, which determines the sampling time of the calculation. Also,

$$\begin{aligned}\boldsymbol{\eta}_1&=f(t_n,\mathbf{X}_n,\mathbf{V}_n),\\ \boldsymbol{\eta}_2&=f\left(t_n+\frac{h}{2},\mathbf{X}_n+\frac{h}{2}\mathbf{V}_n,\mathbf{V}_n+\frac{h}{2}\boldsymbol{\eta}_1\right),\\ \boldsymbol{\eta}_3&=f\left(t_n+\frac{h}{2},\mathbf{X}_n+\frac{h}{2}\mathbf{V}_n+\frac{h^2}{4}\boldsymbol{\eta}_1,\mathbf{V}_n+\frac{h}{2}\boldsymbol{\eta}_2\right),\\ \boldsymbol{\eta}_4&=f\left(t_n+h,\mathbf{X}_n+h\mathbf{V}_n+\frac{h^2}{2}\boldsymbol{\eta}_2,\mathbf{V}_n+h\boldsymbol{\eta}_3\right).\end{aligned}$$

5 Dynamic model of the feed cabin

The feed cabin is composed of the A–B rotator and the SAS. In order to obtain the dynamic model, the kinematic parameters are deduced firstly. Since the two parts are arranged in series, the kinematic parameters are deduced in the order from the A–B rotator to the SAS.

5.1 Kinematics of the feed cabin

The framework is composed of the square frame and four rotation modules. The local frame $\{\boldsymbol{L}_f\}$ of the framework is established as shown in Fig. 10. Another local frame $\{\boldsymbol{L}_S\}$ is established at the geometric center of the square frame, parallel to $\{\boldsymbol{L}_f\}$. Symbol $\mathbf{e}_f$ is the centroid vector of the framework in $\{\boldsymbol{L}_S\}$, while symbol $\mathbf{t}_f$ is the translation vector of $\{\boldsymbol{L}_S\}$ in $\{\boldsymbol{L}_f\}$. Then, the centroid vector can be described under the middle frame as

$${}^{M}\boldsymbol{\kappa}_f={}^{G}\mathbf{R}_f(\mathbf{t}_f+\mathbf{e}_f), \tag{13}$$

where

$${}^{G}\mathbf{R}_f={}^{G}\mathbf{R}_C\cdot{}^{C}\mathbf{R}_f,\qquad {}^{C}\mathbf{R}_f=\begin{bmatrix}c\theta_B & 0 & s\theta_B\\ 0 & 1 & 0\\ -s\theta_B & 0 & c\theta_B\end{bmatrix},$$

$$\mathbf{t}_f=[0,0,t_{fz}]^{\mathrm{T}},$$

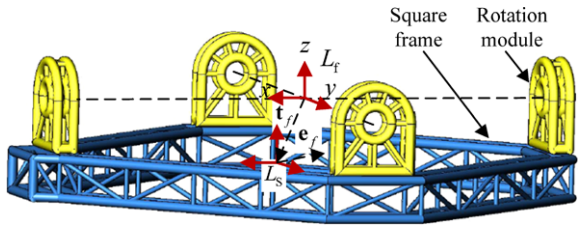

Fig. 10 The sketch map of the framework

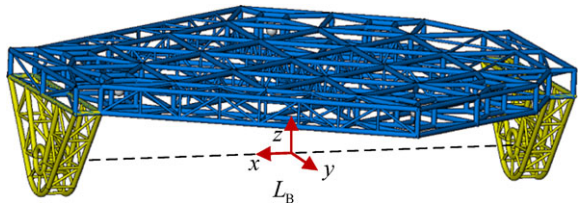

Fig. 11 The sketch map of the SAS base

and θ_B is the rotation angle of the B-axis. Symbol c stands for cosine operation, while s stands for sine operation.

The angular velocity and angular acceleration functions of the framework can be described in the middle frame as

$${}^{M}\boldsymbol{\omega}_f={}^{G}\boldsymbol{\omega}_f={}^{G}\mathbf{R}_C\cdot\dot{\boldsymbol{\xi}}_B, \tag{14}$$

$${}^{M}\boldsymbol{\varepsilon}_f={}^{G}\boldsymbol{\varepsilon}_f={}^{G}\mathbf{R}_C\cdot\ddot{\boldsymbol{\xi}}_B, \tag{15}$$

where $\dot{\boldsymbol{\xi}}_B=[0,\dot{\theta}_B,0]^{\mathrm{T}}$, $\ddot{\boldsymbol{\xi}}_B=[0,\ddot{\theta}_B,0]^{\mathrm{T}}$, and $\dot{\theta}_B$, $\ddot{\theta}_B$ are the rotation velocity and acceleration of the B-axis.

Therefore, the velocity and acceleration of the centroid of the framework in middle frame can be expressed as

$$\begin{aligned}{}^{M}\mathbf{v}_f&={}^{G}\boldsymbol{\omega}_f\times{}^{M}\boldsymbol{\kappa}_f,\\ {}^{M}\mathbf{a}_f&={}^{G}\boldsymbol{\varepsilon}_f\times{}^{M}\boldsymbol{\kappa}_f+{}^{G}\boldsymbol{\omega}_f\times\left({}^{G}\boldsymbol{\omega}_f\times{}^{M}\boldsymbol{\kappa}_f\right).\end{aligned} \tag{16}$$

The moment of inertia $\mathbf{I}_{fo}$ of the framework is defined in $\{\boldsymbol{L}_S\}$, relative to its centroid. The moment of inertia of the framework can be described in $\{\boldsymbol{M}\}$ as

$$\mathbf{I}_f={}^{G}\mathbf{R}_f\mathbf{I}_{fo}{}^{G}\mathbf{R}_f^{\mathrm{T}}. \tag{17}$$

As shown in Fig. 11, the local frame $\{\boldsymbol{L}_B\}$ of the SAS base is attached to the intersection of revolution axes of the A–B rotator, parallel to $\{\boldsymbol{B}\}$. If $\mathbf{t}_B$ is the translation vector that describes the location position of $\{\boldsymbol{B}\}$ in $\{\boldsymbol{L}_B\}$, it can be described under the middle

frame by rotation matrices and translation vectors as

$$^{M}\mathbf{t}_B = {}^{G}\mathbf{R}_B \cdot \mathbf{t}_B, \tag{18}$$

where

$$^{G}\mathbf{R}_B = {}^{G}\mathbf{R}_C \cdot {}^{C}\mathbf{R}_B, \qquad {}^{C}\mathbf{R}_B = \mathbf{R}(Y,\theta_B)\mathbf{R}(X,\theta_A) = \begin{bmatrix} c\theta_B & c\theta_B s\theta_A & s\theta_B c\theta_A \\ 0 & c\theta_A & -s\theta_A \\ -s\theta_B & c\theta_B s\theta_A & c\theta_B c\theta_A \end{bmatrix},$$

and θ_A is the rotation angle of the A-axis.

As $\mathbf{e}_B$ is the position vector of the mass center of the SAS base in $\{\boldsymbol{B}\}$, the position vector of the centroid of the SAS base in $\{\boldsymbol{M}\}$ can be obtained as

$$^{M}\boldsymbol{\kappa}_B = {}^{G}\mathbf{R}_B(\mathbf{t}_B + \mathbf{e}_B), \tag{19}$$

where $\mathbf{t}_B = [0, 0, t_{Bz}]^{\mathrm{T}}$.

The angular velocity and angular acceleration functions of the SAS base can be found in the middle frame as

$$^{M}\boldsymbol{\omega}_B = {}^{G}\boldsymbol{\omega}_B = {}^{G}\mathbf{R}_C\big(\dot{\boldsymbol{\xi}}_B + {}^{C}\mathbf{R}_f \cdot \dot{\boldsymbol{\xi}}_A\big), \tag{20}$$

$$^{M}\boldsymbol{\varepsilon}_B = {}^{G}\boldsymbol{\varepsilon}_B = {}^{G}\mathbf{R}_C\big[\ddot{\boldsymbol{\xi}}_B + {}^{C}\mathbf{R}_f \cdot \ddot{\boldsymbol{\xi}}_A + \dot{\boldsymbol{\xi}}_B \times \big({}^{C}\mathbf{R}_f \cdot \dot{\boldsymbol{\xi}}_A\big)\big], \tag{21}$$

where $\dot{\boldsymbol{\xi}}_A = [\dot{\theta}_A, 0, 0]^{\mathrm{T}}$, $\ddot{\boldsymbol{\xi}}_A = [\ddot{\theta}_A, 0, 0]^{\mathrm{T}}$, and $\dot{\theta}_A$, $\ddot{\theta}_A$ are the rotation velocity and acceleration of the A-axis; $\dot{\boldsymbol{\xi}}_B\times$ can be described by the skew-symmetric operator as $\dot{\boldsymbol{\xi}}_B\times = {}^{C}\dot{\mathbf{R}}_f \cdot {}^{C}\mathbf{R}_f^{\mathrm{T}}$.

Similarly, the acceleration of the centroid of the SAS base in the middle frame is

$$\begin{aligned} ^{M}\mathbf{v}_B &= {}^{G}\boldsymbol{\omega}_B \times {}^{M}\boldsymbol{\kappa}_B, \\ ^{M}\mathbf{a}_B &= {}^{G}\boldsymbol{\varepsilon}_B \times {}^{M}\boldsymbol{\kappa}_B + {}^{G}\boldsymbol{\omega}_B \times \big({}^{G}\boldsymbol{\omega}_B \times {}^{M}\boldsymbol{\kappa}_B\big). \end{aligned} \tag{22}$$

The acceleration of the SAS base frame can be derived in the global frame as

$$^{G}\ddot{\mathbf{t}}_B = {}^{G}\ddot{\mathbf{t}}_M + {}^{M}\ddot{\mathbf{t}}_B, \tag{23}$$

where

$$^{M}\ddot{\mathbf{t}}_B = {}^{G}\boldsymbol{\varepsilon}_B \times {}^{M}\mathbf{t}_B + {}^{G}\boldsymbol{\omega}_B \times \big({}^{G}\boldsymbol{\omega}_B \times {}^{M}\mathbf{t}_B\big). \tag{24}$$

The moment of inertia $\mathbf{I}_{Bo}$ of the SAS base is defined in $\{\boldsymbol{B}\}$, relative to its centroid. The moment of inertia can be obtained in $\{\boldsymbol{M}\}$ as

$$\mathbf{I}_B = {}^{G}\mathbf{R}_B \mathbf{I}_{Bo} {}^{G}\mathbf{R}_B^{\mathrm{T}}. \tag{25}$$

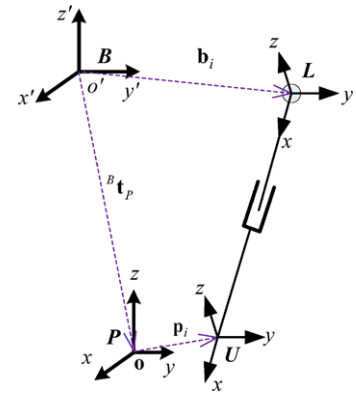

Fig. 12 Kinematic model of the ith SAS leg

The kinematic model of the ith SAS leg is shown in Fig. 12. Two local frames denoted as $\{\boldsymbol{L}\}$ and $\{\boldsymbol{U}\}$ are established in the leg. Frame L is attached to the SAS base point B_i (the rotation center of the universal joint of the leg), with the x-axis along the leg. The cross product of the x-axis of frame L and the location vector of the SAS base point B_i is defined as the y-axis of frame L. Then, the z-axis is easy to obtain by the cross product of x-axis and y-axis. Frame U is attached to the SAS end-effector point P_i (the rotation center of the universal joint of the leg), parallel to the local frame L. Translational frames $\{\boldsymbol{L}'\}$ and $\{\boldsymbol{P}'\}$ are introduced (not shown separately in Fig. 12), parallel to the global frame. $\{\boldsymbol{L}'\}$ is attached to the origin point of $\{\boldsymbol{L}\}$, while $\{\boldsymbol{P}'\}$ is attached to the origin point of $\{\boldsymbol{P}\}$.

Since kinematic derivation of the SAS is similar to that of the A–B rotator, the procedure is omitted here and demonstrated in Appendix A. The derivation procedure of the feed cabin dynamics is carried out in the order from the SAS to the A–B rotator.

5.2 Dynamics of the feed cabin

In $\{\boldsymbol{L}'\}$, relative to the SAS base point B_i, the Euler's equation for the entire limb of the SAS is deduced as

$$\begin{aligned} &{}^{G}\mathbf{S}_i \times \mathbf{F}_{Si} + M_{Ui}\,{}^{G}\mathbf{s}_i \\ &\quad = m_L \mathbf{r}_{Li} \times \mathbf{a}_{Li} + m_U \mathbf{r}_{Ui} \times \mathbf{a}_{Ui} + (\mathbf{I}_{Li} + \mathbf{I}_{Ui})\,{}^{G}\mathbf{A}_i \\ &\qquad + {}^{G}\mathbf{W}_i \times (\mathbf{I}_{Li} + \mathbf{I}_{Ui})\,{}^{G}\mathbf{W}_i \\ &\qquad + (m_L \mathbf{r}_{Li} + m_U \mathbf{r}_{Ui}) \times \mathbf{a}_{Lri} \\ &\qquad - (m_L \mathbf{r}_{Li} + m_U \mathbf{r}_{Ui}) \times \mathbf{g} \end{aligned}$$

where M_{Ui} is the mode of the constrained torque exerted by the universal joint avoiding rotation along the limb axis, and $\mathbf{F}_{Si}$ is the constrained force of the spherical joints acting on the limb.

By taking cross products of both sides with ${}^{G}\mathbf{s}_i$, the above equation can be simplified as

$$ {}^{G}\mathbf{F}_{Si} = \boldsymbol{C}_i + (F_{\mathrm{Leg}})_i {}^{G}\mathbf{s}_j, \tag{26} $$

where

$$ \boldsymbol{C}_i = \frac{\mathbf{D}_i \times {}^{G}\mathbf{s}_i}{L_i}, $$

$$ (F_{\mathrm{Leg}})_i = {}^{G}\mathbf{s}_i \cdot {}^{G}\mathbf{F}_{Si}, $$

$$ \begin{aligned} \mathbf{D}_i = {} & m_L \mathbf{r}_{Li} \times \mathbf{a}_{Li} + m_U \mathbf{r}_{Ui} \times \mathbf{a}_{Ui} + (\mathbf{I}_{Li} + \mathbf{I}_{Ui}) {}^{G}\mathbf{A}_i \\ & + {}^{G}\mathbf{W}_i \times (\mathbf{I}_{Li} + \mathbf{I}_{Ui}) {}^{G}\mathbf{W}_i \\ & + (m_L \mathbf{r}_{Li} + m_U \mathbf{r}_{Ui}) \times \mathbf{a}_{Lri} \\ & - (m_L \mathbf{r}_{Li} + m_U \mathbf{r}_{Ui}) \times \mathbf{g}. \end{aligned} $$

As the reaction force of ${}^{G}\mathbf{F}_{Si}$ is exerted on the SAS end effector, the Newton's equation for the FSS terminal can be written as

$$ m_P \mathbf{g} - \sum_{i=1}^{6} {}^{G}\mathbf{F}_{Si} - m_P \mathbf{a}_{Pr} = m_P \mathbf{a}_P. \tag{27} $$

Relative to the geometric center, the Euler's equation for the FSS terminal can be written as

$$ \begin{aligned} & m_P {}^{G}\mathbf{e} \times \mathbf{g} - \sum_{i=1}^{6} \left({}^{G}\mathbf{R}_C \cdot {}^{C}\mathbf{R}_B \cdot {}^{B}\mathbf{R}_P \cdot \mathbf{p}_i \right) \times {}^{G}\mathbf{F}_{Si} \\ & \quad - m_P {}^{G}\mathbf{e} \times \mathbf{a}_{Pr} \\ & = m_P {}^{G}\mathbf{e} \times \mathbf{a}_P + {}^{G}\boldsymbol{\varepsilon}_P \mathbf{I}_P + {}^{G}\boldsymbol{\omega}_P \times \left(\mathbf{I}_P \cdot {}^{G}\boldsymbol{\omega}_P \right). \end{aligned} \tag{28} $$

Substituting $({}^{G}\mathbf{F}_S)_i$ into Eq. (26), $(F_{\mathrm{Leg}})_i$ can be obtained from the Newton and Euler equations listed above. Organizing the equations in matrix form, we obtain

$$ \mathbf{H} \cdot \mathbf{F}_{\mathrm{Leg}} = \mathbf{N}, \tag{29} $$

where

$$ \mathbf{H} = \begin{bmatrix} {}^{G}\mathbf{s}_1 & {}^{G}\mathbf{s}_2 & {}^{G}\mathbf{s}_3 & {}^{G}\mathbf{s}_4 & {}^{G}\mathbf{s}_5 & {}^{G}\mathbf{s}_6 \\ \boldsymbol{\rho}_1 & \boldsymbol{\rho}_2 & \boldsymbol{\rho}_3 & \boldsymbol{\rho}_4 & \boldsymbol{\rho}_5 & \boldsymbol{\rho}_6 \end{bmatrix}, $$

$$ \boldsymbol{\rho}_i = \left({}^{G}\mathbf{R}_C \cdot {}^{C}\mathbf{R}_B \cdot {}^{B}\mathbf{R}_P \cdot \mathbf{p}_i \right) \times {}^{G}\mathbf{s}_i \quad i = 1, 2, \ldots, 6, $$

$$ \mathbf{F}_{\mathrm{Leg}} = \left[(F_{\mathrm{Leg}})_1, (F_{\mathrm{Leg}})_2, (F_{\mathrm{Leg}})_3, (F_{\mathrm{Leg}})_4, (F_{\mathrm{Leg}})_5, (F_{\mathrm{Leg}})_6 \right]^{\mathrm{T}}, $$

$$ \mathbf{N} = \begin{bmatrix} m_P \mathbf{g} - \sum_{i=1}^{6} \mathbf{C}_i - m_P \mathbf{a}_{Pr} - m_P \mathbf{a}_P \\ m_P {}^{G}\mathbf{e} \times (\mathbf{g} - \mathbf{a}_P - \mathbf{a}_{Pr}) - \mathbf{I}_P \cdot {}^{G}\boldsymbol{\varepsilon}_P - \sum_{i=1}^{6} {}^{G}\mathbf{R}_B \cdot {}^{B}\mathbf{R}_P \cdot \mathbf{P}_i \times \boldsymbol{C}_i - {}^{G}\boldsymbol{\omega}_P \times (\mathbf{I}_P \cdot {}^{G}\boldsymbol{\omega}_P) \end{bmatrix}. $$

The Newton's equation of the upper part of the SAS limb gives

$$ {}^{G}\mathbf{F}_{Si} = m_U \mathbf{g} - \mathbf{F}_{PJi} = m_U (\mathbf{a}_{Ui} + \mathbf{a}_{Lri}), $$

where $\mathbf{F}_{PJi}$ is the sum of the driving and constrained forces of prismatic joint of the ith limb. Since the driving force is along the limb axis, taking the dot product with the limb unit vector ${}^{G}\mathbf{s}_i$ gives

$$ F_i = (F_{\mathrm{Leg}})_i + U_i, $$

where

$$ \begin{aligned} F_i &= {}^{G}\mathbf{s}_i \cdot \mathbf{F}_{PJi}, \\ U_i &= m_U {}^{G}\mathbf{s}_i \cdot \left[\mathbf{g} - (\mathbf{a}_{Ui} + \mathbf{a}_{Lri}) \right], \end{aligned} \tag{30} $$

and F_i is the driving force of prismatic joint. The required input forces can be determined in matrix form as

$$ \mathbf{F} = \mathbf{F}_{\mathrm{Leg}} + \mathbf{U}, \tag{31} $$

where

$$\mathbf{F} = [F_1, F_2, F_3, F_4, F_5, F_6]^{\mathrm{T}}$$

and

$$\boldsymbol{U} = [U_1, U_2, U_3, U_4, U_5, U_6]^{\mathrm{T}}.$$

In order to determine the force of the universal joint acting on the limb, the Newton's equation for the entire SAS limb in global frame is written as

$$\begin{aligned} &{}^{G}\mathbf{F}_{Ui} + {}^{G}\mathbf{F}_{Si} + (m_L + m_U)\mathbf{g} \\ &\quad = m_L(\mathbf{a}_{Li} + \mathbf{a}_{Lri}) + m_U(\mathbf{a}_{Ui} + \mathbf{a}_{Lri}), \end{aligned} \tag{32}$$

where ${}^{G}\mathbf{F}_{Ui}$ is the force exerted by the universal joint to the limb.

On the basis of the SAS dynamics, the dynamics of the A–B rotator are derived. The Newton's equation for the SAS base in global frame gives

$$\mathbf{F}_A - \sum_{i=1}^{6} {}^{G}\mathbf{F}_{Ui} + m_B\mathbf{g} = m_B\left({}^{G}\ddot{\mathbf{t}}_M + {}^{M}\mathbf{a}_B\right), \tag{33}$$

where $\mathbf{F}_A$ is the force exerted by the framework to the SAS base, and m_B is the mass of the SAS base. Taking the moment acting on the SAS base in the middle frame about the intersection point of revolution axes in A–B rotator, the Euler's equation gives

$$\begin{aligned} &\mathbf{M}_A - \sum_{i=1}^{6}\left({}^{M}\mathbf{t}_{bi} \times {}^{G}\mathbf{F}_{Ui}\right) \\ &\qquad + m_B{}^{M}\boldsymbol{\kappa}_B \times \left(\mathbf{g} - {}^{G}\ddot{\mathbf{t}}_M - {}^{M}\mathbf{a}_b\right) \\ &\quad = \mathbf{I}_B \cdot {}^{M}\boldsymbol{\varepsilon}_B + {}^{M}\boldsymbol{\omega}_B \times \left(\mathbf{I}_B \cdot {}^{M}\boldsymbol{\omega}_B\right), \end{aligned} \tag{34}$$

where $\mathbf{M}_A$ is the torque exerted by the framework to the SAS base.

The Newton's equation for the framework in global frame can be written as

$$\mathbf{F}_B - \mathbf{F}_A + m_F\mathbf{g} = m_F\left({}^{G}\ddot{\mathbf{t}}_M + {}^{M}\mathbf{a}_f\right), \tag{35}$$

where $\mathbf{F}_B$ is the force exerted by the base of the cable-driven Stewart manipulator to the framework, and m_F is the mass of the framework. The Euler's equation for the framework about the intersection point of revolution axes in A–B rotator in the middle frame gives

$$\begin{aligned} &\mathbf{M}_B - \boldsymbol{M}_A + m_F{}^{M}\boldsymbol{\kappa}_f \times \left(\mathbf{g} - {}^{G}\ddot{\mathbf{t}}_M - {}^{M}\mathbf{a}_f\right) \\ &\quad = \mathbf{I}_f \cdot {}^{M}\boldsymbol{\varepsilon}_f + {}^{M}\boldsymbol{\omega}_f \times \left(\mathbf{I}_f \cdot {}^{M}\boldsymbol{\omega}_f\right), \end{aligned} \tag{36}$$

where $\mathbf{M}_B$ is the torque exerted by the base of the cable-driven Stewart manipulator to the framework.

Now, the dynamic equations of the feed cabin are accomplished, involving non-inertial coordinate system and the Stewart manipulator with a moving base. The internal forces and torques of the feed cabin are deduced.

6 Frequency and stiffness analysis

In order to study the frequency and stiffness features of the FSS, the external step forces and torques are exerted on the cable platform along translation axes and rotation axes of the global frame, respectively. According to Eq. (12) and the recurrence formulas of the Runge–Kutta method, the position and orientation offset of the cable platform can be calculated. And, simulation results are shown in Fig. 13. The simulation step is 0.01 s.

According to the step response of the FSS, the vibration frequency along Z-axis is about 0.55 Hz, which is a little higher than frequencies along X-axis (about 0.24 Hz) and Y-axis (about 0.3 Hz). The vibration frequency along C-axis is around 0.84 Hz, which is higher than frequencies along A-axis (about 0.3 Hz) and B-axis (about 0.24 Hz). So, the lowest vibration frequency of the FSS is about 0.24 Hz. According to the Davenport spectrum, the wind effect around this frequency takes up only a small fraction of the overall wind power.

The step force acting on the FSS is 500 N while the step torque is 500 N m. The stiffness of three translation orientations is all greater than 10^5 N m^{-1}. The stiffness of the Z-axis is slightly higher than that of X-axis and Y-axis. The same phenomenon is observed in three rotation directions, whose stiffness is greater than 10^6 N m rad^{-1}. To sum up, the stiffness of the FSS is quite low and destined to produce noticeable position error under the wind disturbance (wind force is beyond 10^3 N). In order to determine the practical terminal error of the FSS, the wind vibration simulation is carried out in the next section.

7 Wind vibration simulation of the FSS

In this section, the wind vibration simulation of the FSS is carried out, adopting the dynamic model of the

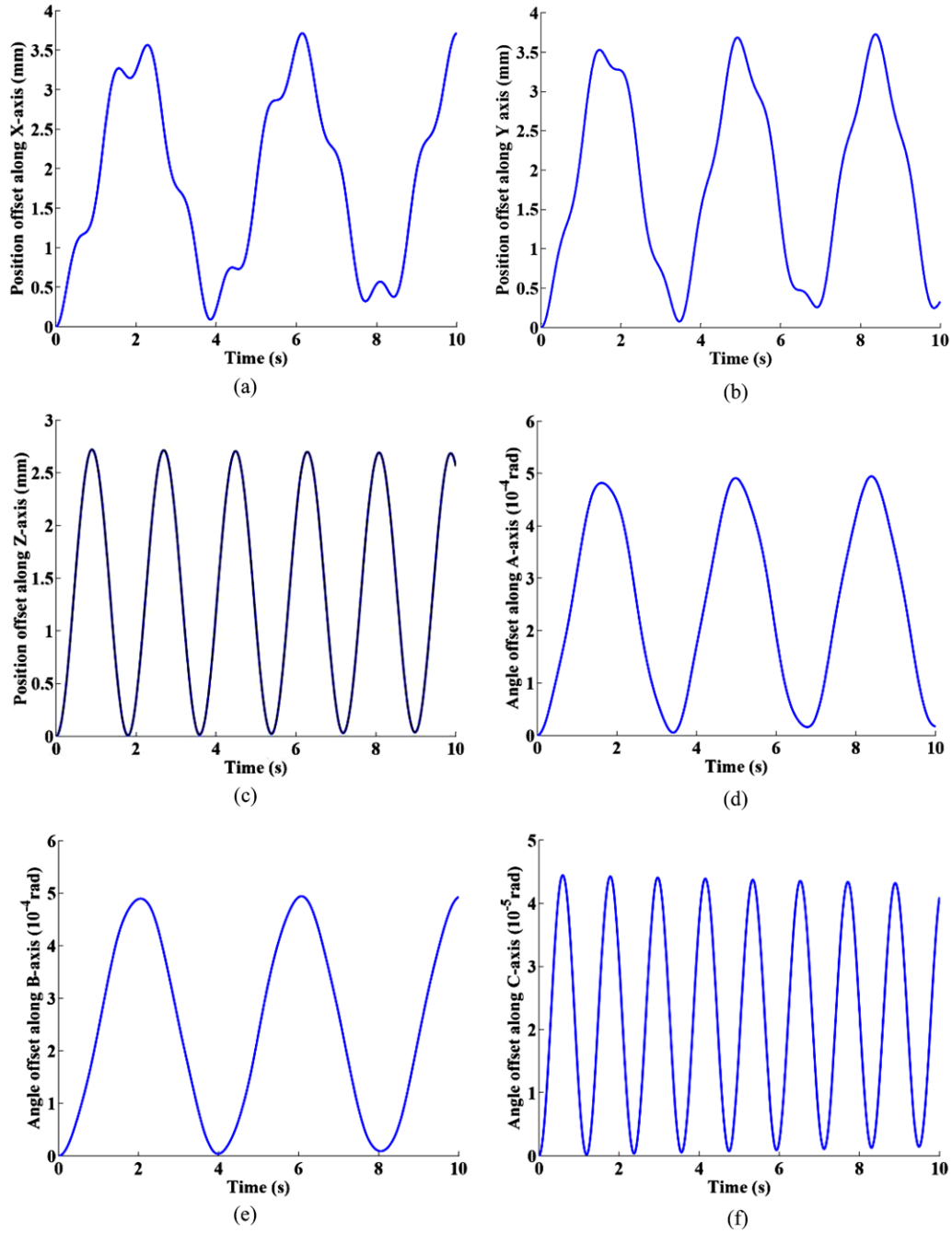

Fig. 13 Step responses of the FSS: (**a**) position offset along X-axis, (**b**) position offset along Y-axis, (**c**) position offset along Z-axis, (**d**) angle offset along A-axis, (**e**) angle offset along B-axis, (**f**) angle offset along C-axis

cable-driven Stewart manipulator and the wind disturbance model, obtained in Sects. 3 and 4. The wind force is exerted on the center of the cable platform along the X-axis in the global frame. The dynamic responses of the cable platform and the FSS terminal (the SAS end effector) are shown in Figs. 14 and 15, respectively.

The main direction of the vibration is along X-axis. As there is a distance (7 m at initial state) between the cable platform and the FSS terminal, the terminal er-

ror will be amplified by the rotation of the cable platform along the B-axis. The maximum position offset of the center of the cable platform is about 31.16 mm while the maximum terminal position offset reaches up to 82.14 mm. The FSS terminal error is far beyond the accuracy requirement. So, in the next section, the vibration control strategies of the SAS are proposed to improve the terminal accuracy, and simulations are carried out.

8 Vibration control strategies

The accuracy requirement of the FSS is that the terminal error is not more than 10 mm in RMS. The rigid Stewart manipulator (SAS) is used to reduce the terminal error resulted from the vibration induced by the wind force, to improve the terminal positioning accuracy. The A–B rotator and the cable-driven Stewart are controlled according to the path plan to realize the observation motion. The block diagram of the FSS control system is shown in Fig. 16. In order to focus on the vibration control strategy, a target position and posture are used instead of the target trajectory. Then, the path plan can be omitted. The simulation model is simplified as demonstrated in the dashed box in Fig. 16. In the following simulation, the initial state of the FSS is used as the target position and posture, such as ${}^{G}\mathbf{t}_P = [0, 0, 140]^{\mathrm{T}}$ and ${}^{G}\boldsymbol{\theta}_P = [0, 0, 0]^{\mathrm{T}}$. Two different vibration control strategies, kinematic vibration compensation and dynamic vibration suppression, are simulated and evaluated.

8.1 Kinematic vibration compensation

The SAS can be controlled to compensate the terminal error resulting from the vibration of the cable-driven

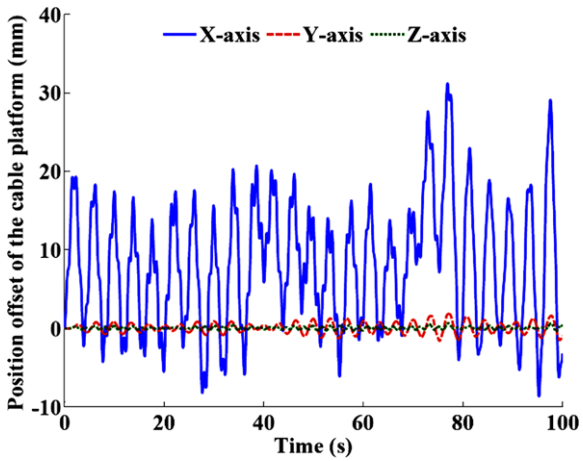

Fig. 14 Position offset of the cable platform under wind disturbance

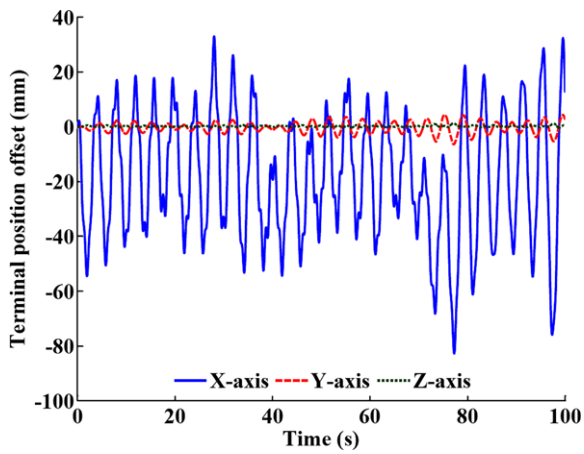

Fig. 15 Terminal position offset of the FSS under wind disturbance

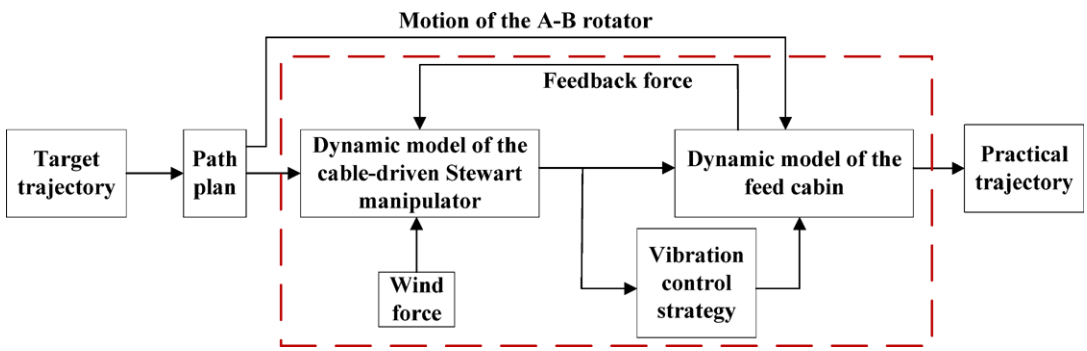

Fig. 16 Block diagram of the FSS control system

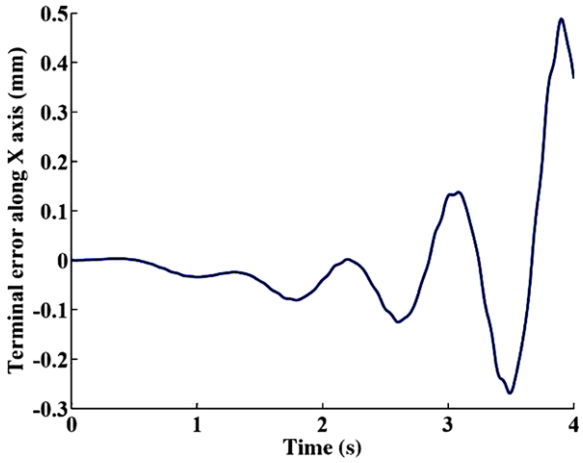

Fig. 17 Terminal error along X-axis with kinematic vibration compensation

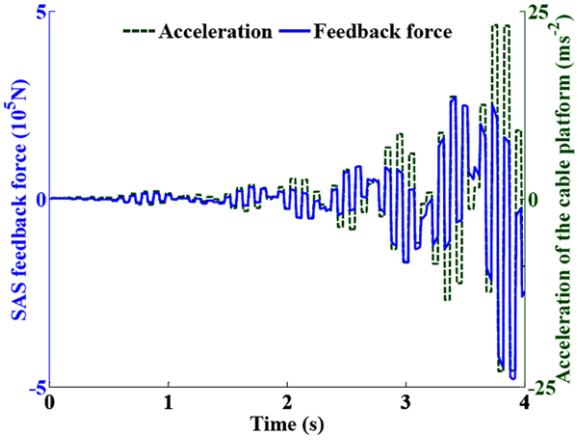

Fig. 18 The SAS feedback force and the acceleration of the cable platform in X-axis

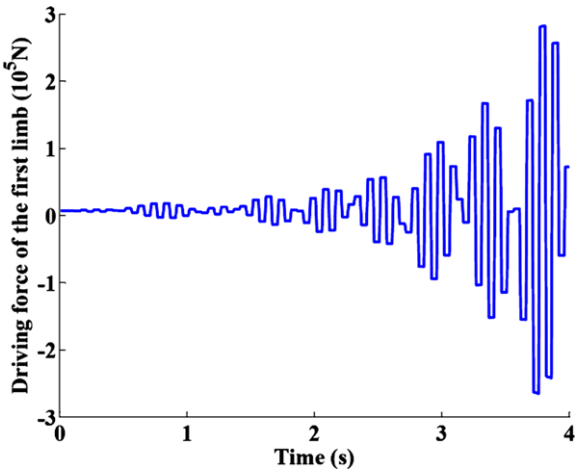

Fig. 19 Driving force of the first SAS limb

Stewart manipulator. In this case, the real-time measurement of position and posture is inevitable. Since the FSS terminal is covered in the feed cabin shield, the FSS terminal position and posture in the global frame are hard to measure. The position and posture of the feed cabin are measured instead, which can be converted to the position and posture of the cable platform easily. The kinematic vibration compensation strategy can be subdivided into three steps. First, calculate the practical terminal error on the basis of the position and posture of the cable platform obtained by measurement. Then, figure out the required movement of each SAS limb to compensate the terminal error. Finally, execute the required movement of each limb in the next control cycle, and the constant acceleration strategy is used. Considering the practical limits of non-contact measurement equipments, the highest measuring frequency is assumed as 10 Hz. The simulation result of the FSS terminal error along X-axis is shown in the Fig. 17.

As shown in the figure, the FSS terminal error is far from being controlled. In order to analyze the reason of the vibration divergence, the feedback force of the SAS and the acceleration of the cable platform along X-axis are calculated as shown in Fig. 18. The feedback force generated by the kinematic compensation of the SAS is united in action with the cable-platform acceleration. As the result, larger vibration is brought in, which needs faster motion of the SAS to compensate for the terminal error. However, faster motion leads to larger feedback force. This vicious circle goes on, and the feedback force soon surpasses the wind disturbance, becoming the main excitation source for the FSS vibration. At the same time, the limb driving forces of the SAS increase sharply. Driving force of the first limb is calculated and shown in Fig. 19.

After all, since the FSS terminal weighs more than 3 ton, the feedback force is considerable and has a significant impact on the vibration of the FSS. In the next section, the feedback force is used to suppress the system vibration through controlling the SAS acceleration.

8.2 Dynamic vibration suppression

In the dynamic vibration suppression strategy, the SAS feedback force is used to counteract the external wind disturbance. In practical application, the strategy

is achieved though controlling the SAS acceleration according to the acceleration of the cable platform, which is the direct reflection of the external disturbance. The cable-platform acceleration can be measured by an accelerometer in real time. The measuring frequency is assumed as 100 Hz. A simple proportional control is used to determine the required SAS acceleration, which can be expressed in the SAS base frame as

$$
{}^{B}\ddot{\mathbf{t}}_P = \lambda\left({}^{G}\mathbf{R}_C \cdot {}^{C}\mathbf{R}_B\right)^{\mathrm{T}}\,{}^{G}\ddot{\mathbf{t}}_C,
$$

$$
{}^{B}\ddot{\boldsymbol{\theta}}_P = \lambda\left({}^{G}\mathbf{R}_C \cdot {}^{C}\mathbf{R}_B\right)^{\mathrm{T}}\,{}^{G}\ddot{\boldsymbol{\theta}}_C,
$$

where λ is the acceleration proportional gain. In order to find the right acceleration ratio, the terminal error along X-axis with different ratio is figured out as shown in Fig. 20. According to the figure, the minimum terminal error in RMS is obtained when the proportional gain is 2.6.

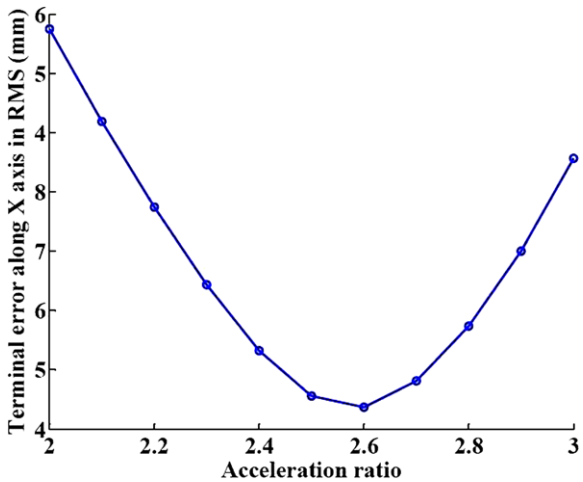

Fig. 20 Terminal error with different acceleration ratio

When $\lambda = 2.6$, the acceleration of the cable platform and the SAS feedback force along X-axis are shown in Fig. 21. Direction of the feedback force maintains the opposite of the acceleration direction at all times, which effectively suppresses the FSS vibration. As a result, the FSS terminal error is greatly reduced. The terminal error under the dynamic vibration suppression is shown in Fig. 22. Since the wind force is exerted onto the FSS along X-axis, the maximum terminal error appears along the X-axis. The terminal errors along Y-axis and Z-axis are relatively small. The overall FSS terminal error is 4.3 mm in RMS, which meets well the accuracy requirement (10 mm in RMS).

The driving forces of the SAS are shown in Fig. 23. The driving force of each limb changes around the initial value without large deviation, which means that the SAS performs well.

The compensation motion of the SAS is shown in Fig. 24. The maximum displacement is about 50 mm, occurring along x'-axis in the SAS base frame. The designed workspace of the SAS is a sphere with the radius of 250 mm.

In brief, the dynamic vibration suppression strategy proposed above can meet the required FSS terminal accuracy. Besides, the driving forces of the SAS are reasonable and the SAS motion is within the designed workspace. Thus, the dynamic vibration suppression can be adopted in the vibration control of the FAST prototype.

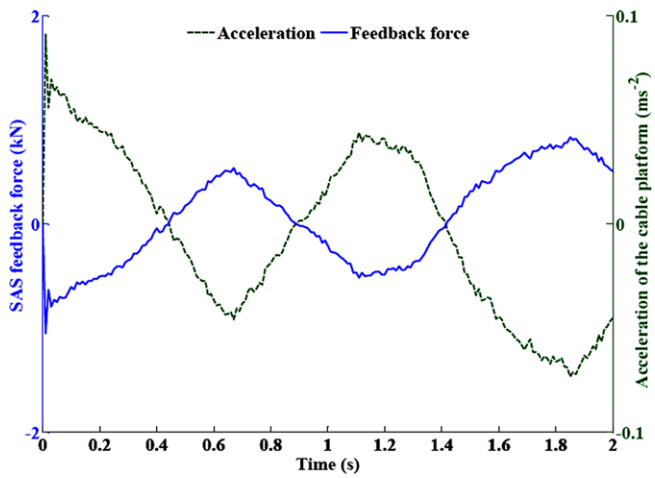

Fig. 21 Acceleration of the cable platform and the SAS feedback force along X-axis

9 Conclusion

In this article, the rigid dynamic model of the feed cabin in FAST is derived. The derived dynamic equation involves complex hybrid manipulator, which consists of an A–B rotator and a rigid Stewart manipulator (SAS). The elastic dynamic model of the cable-driven Stewart manipulator is deduced by simplifying the driving cable as the spring damping model. On the basis of the Davenport filter, a sample of the FSS wind force is deduced. Finally, the simulation model of the FSS is established. The vibration and stiffness characteristics of the FSS are analyzed. The lowest nature frequency is 0.24 Hz, which misses the main fraction of the total wind power. However, the terminal error of FSS under the wind disturbance is noticeable, because of low stiffness.

The kinematic vibration compensation and dynamic vibration suppression strategies are simulated and evaluated though the deduced FSS dynamic model. With the kinematic vibration compensation strategy, the SAS feedback force becomes a vibration excitation and enlarges the FSS terminal error. On the contrary, the dynamic vibration suppression strategy makes full use of the SAS feedback force to suppress the FSS vibration, and reduces the terminal error to 4.3 mm in RMS, which meets the accuracy requirement well. Besides, the SAS driving forces are mild, and the SAS motion is far from the workspace edge. Thus, the dynamic vibration suppression strategy is proved to be a satisfying way to improve the FSS ter-

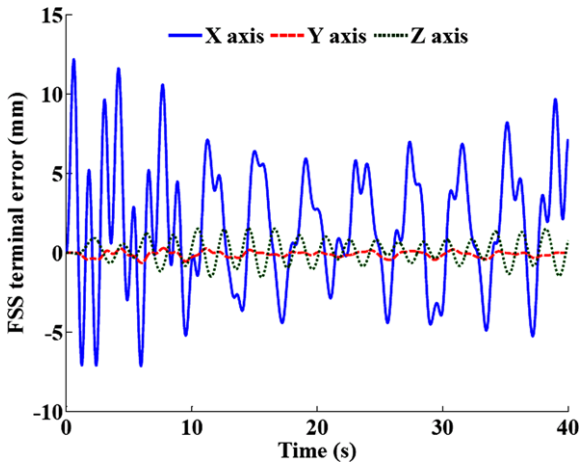

Fig. 22 FSS terminal errors when $\lambda = 2.6$

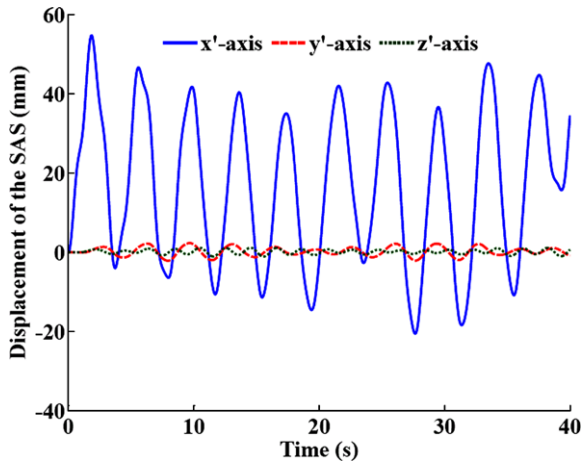

Fig. 24 SAS motion in dynamic vibration suppression

Fig. 23 Driving forces of the SAS

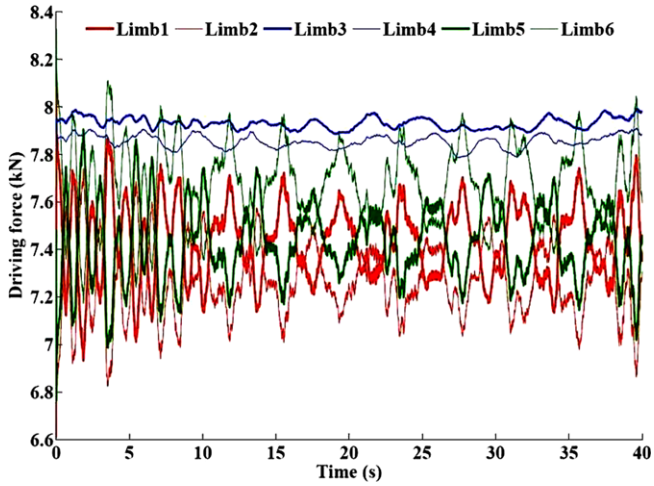

minal accuracy, and should be adopted in the control of the FAST prototype.

Acknowledgements This research is sponsored by the National Natural Science Foundation of China (No. 50975149), the National 973 Program of China (No. 2007CB714007), and the Important National Science and Technology Specific Projects of China (No. 2009ZX04001-042-02).

Appendix A: Detailed derivation of the SAS kinematics

The SAS base point B_i $(i = 1, 2, \ldots, 6)$ can be described under the middle frame by rotation matrices and translation vectors as

$$^{M}\mathbf{t}_{bi} = {}^{M}\mathbf{t}_{B} + {}^{G}\mathbf{R}_{C} \cdot {}^{C}\mathbf{R}_{B} \cdot \mathbf{b}_{i}. \tag{A.1}$$

The SAS end-effector point P_i $(i = 1, 2, \ldots, 6)$ can be also expressed in middle frame as

$$^{M}\mathbf{t}_{pi} = {}^{M}\mathbf{t}_{P} = {}^{G}\mathbf{R}_{C} \cdot {}^{B}\mathbf{R}_{P} \cdot \mathbf{p}_{i}, \tag{A.2}$$

where

$$^{M}\mathbf{t}_{P} = {}^{M}\mathbf{t}_{B} + {}^{G}\mathbf{R}_{C} \cdot {}^{C}\mathbf{R}_{B} \cdot {}^{B}\mathbf{t}_{P}, \tag{A.3}$$

$$\begin{aligned} &{}^{B}\mathbf{R}_{P} \\ &\quad = \mathbf{R}(z, \phi) \cdot \mathbf{R}(y, \varphi) \cdot \mathbf{R}(x, \psi) \\ &\quad = \begin{bmatrix} c\phi c\varphi & c\phi s\varphi s\psi - s\phi c\psi & c\phi s\varphi c\psi + s\phi s\psi \\ s\phi c\varphi & s\phi s\varphi s\psi + c\phi s\psi & s\phi s\varphi c\psi - c\phi s\psi \\ -s\varphi & c\varphi s\psi & c\varphi c\psi \end{bmatrix} \end{aligned}$$

and ψ, φ, and ϕ are rotation angles of the FSS terminal (SAS end effector) relative to the SAS base.

Then, the leg vector $\mathbf{S}_i$ (from the origin of the frame L to the origin of the frame U) can be derived from the difference of position vectors $\mathbf{p}_i$ and $\mathbf{b}_i$. We can get $\mathbf{S}_i$ under the global fame as

$$^{G}\mathbf{S}_{i} = {}^{M}\mathbf{t}_{pi} - {}^{M}\mathbf{t}_{bi} = {}^{G}\mathbf{R}_{B} \cdot {}^{B}\mathbf{S}_{i}, \tag{A.4}$$

where

$$^{B}\mathbf{S}_{i} = {}^{B}\mathbf{t}_{P} - \mathbf{b}_{i} + {}^{B}\mathbf{R}_{P} \cdot \mathbf{p}_{i}. \tag{A.5}$$

Further, the leg length, which is also the inverse kinematics for the SAS, is obtained as

$$L_i = \left\| {}^{G}\mathbf{S}_{i} \right\|. \tag{A.6}$$

The relation between the unit leg vector and the leg vector can be described under the global frames as

$$^{G}\mathbf{S}_{i} = L_i \, {}^{G}\mathbf{s}_{i}. \tag{A.7}$$

The velocity mapping functions is found in the global frame by taking the derivative of Eqs. (A.4) and (A.7) with respect to time, i.e.,

$$^{G}\dot{\mathbf{S}}_{i} = {}^{G}\boldsymbol{\omega}_{B} \times {}^{G}\mathbf{S}_{i} + {}^{G}\mathbf{R}_{B} \cdot {}^{B}\dot{\mathbf{S}}_{i} \tag{A.8}$$

and

$$^{G}\dot{\mathbf{S}}_{i} = \dot{L}_i \, {}^{G}\mathbf{s}_{i} + L_i \, {}^{G}\mathbf{W}_{i} \times {}^{G}\dot{\mathbf{s}}_{i}, \tag{A.9}$$

where

$$\begin{aligned} &{}^{G}\boldsymbol{\omega}_{B}\times = {}^{G}\dot{\mathbf{R}}_{B} \cdot {}^{G}\mathbf{R}_{B}^{\mathrm{T}}, \\ &{}^{B}\dot{\mathbf{S}}_{i} = {}^{B}\dot{\mathbf{t}}_{P} + {}^{B}\boldsymbol{\omega}_{P} \times \left({}^{B}\mathbf{R}_{P} \cdot \mathbf{P}_{i}\right). \end{aligned}$$

According to the physical meaning, $\dot{L}_i$ is the sliding velocity of the SAS leg, while ${}^{G}\mathbf{W}_i$ is the angular velocity of the SAS leg under the global frame. Taking the dot product of Eq. (34) with ${}^{G}\mathbf{s}_i$, we can obtain

$$\dot{L}_i = {}^{G}\mathbf{s}_{i} \cdot {}^{G}\dot{\mathbf{S}}_{i} = {}^{B}\mathbf{s}_{i} \cdot {}^{B}\dot{\mathbf{S}}_{i}. \tag{A.10}$$

Cross-multiplying both sides of Eq. (A.9) with ${}^{G}\mathbf{s}_i$ gives the angular velocity of the leg as

$$^{G}\mathbf{W}_{i} = {}^{G}\mathbf{s}_{i} \times {}^{G}\dot{\mathbf{S}}_{i} / L_i. \tag{A.11}$$

Similarly, ${}^{G}\ddot{\mathbf{S}}_i$ can be expressed in two ways. By taking the derivative of Eq. (A.8) with respect to time, we can obtain

$$\begin{aligned} {}^{G}\ddot{\mathbf{S}}_{i} = {}&{}^{G}\boldsymbol{\varepsilon}_{B} \times {}^{G}\mathbf{S}_{i} + {}^{G}\boldsymbol{\omega}_{B} \times {}^{G}\dot{\mathbf{S}}_{i} \\ &+ {}^{G}\boldsymbol{\omega}_{B} \times \left({}^{G}\mathbf{R}_{B} \cdot {}^{B}\dot{\mathbf{S}}_{i}\right) \\ &+ {}^{G}\mathbf{R}_{B} \cdot {}^{B}\ddot{\mathbf{S}}_{i}, \end{aligned} \tag{A.12}$$

where

$$\begin{aligned} {}^{B}\ddot{\mathbf{S}}_{i} = {}&{}^{B}\ddot{\mathbf{t}}_{P} + {}^{B}\boldsymbol{\varepsilon}_{P} \times \left({}^{B}\mathbf{R}_{P} \cdot \mathbf{p}_{i}\right) \\ &+ {}^{B}\boldsymbol{\omega}_{P} \times \left[{}^{B}\boldsymbol{\omega}_{P} \times \left({}^{B}\mathbf{R}_{P} \cdot \mathbf{p}_{i}\right)\right]. \end{aligned} \tag{A.13}$$

Either by taking the derivative of Eq. (A.10) or according to the physical meaning, ${}^{G}\ddot{\mathbf{S}}$ can also be described as

$$\begin{aligned} {}^{G}\ddot{\mathbf{S}}_{i} = {}&\ddot{L}_i \, {}^{G}\mathbf{s}_{i} + {}^{G}\mathbf{W}_{i} \times \left({}^{G}\mathbf{W}_{i} \times {}^{G}\mathbf{S}_{i}\right) \\ &+ 2 {}^{G}\mathbf{W}_{i} \times \dot{L}_i \, {}^{G}\mathbf{s}_{i} + {}^{G}\mathbf{A}_{i} \times {}^{G}\mathbf{S}_{i}, \end{aligned} \tag{A.14}$$

which may be simplified as

$$
{}^{G}\ddot{\mathbf{S}}_i = \left(\ddot{L}_i - L_i {}^{G}\mathbf{W}_i \cdot {}^{G}\mathbf{W}_i\right){}^{G}\mathbf{s}_i + 2\dot{L}_i {}^{G}\mathbf{W}_i \times {}^{G}\mathbf{s}_i + {}^{G}\mathbf{A}_i \times {}^{G}\mathbf{S}_i. \tag{A.15}
$$

By taking respectively dot product and cross product at both sides of the above equation with ${}^{G}\mathbf{s}_i$, we obtain the expression of the sliding acceleration $\ddot{L}_i$ and the angular velocity ${}^{G}\mathbf{A}_i$ of the leg in the global frame as

$$
\ddot{L}_i = L_i {}^{G}\mathbf{W}_i \cdot {}^{G}\mathbf{W}_i + {}^{G}\mathbf{s}_i \cdot {}^{G}\ddot{\mathbf{S}}_i \tag{A.16}
$$

and

$$
{}^{G}\mathbf{A}_i = \left({}^{G}\mathbf{s}_i \times {}^{G}\ddot{\mathbf{S}}_i - 2\dot{L}_i {}^{G}\mathbf{W}_i\right)/L_i. \tag{A.17}
$$

The rotation matrix of the ith leg from $\{\boldsymbol{L}\}$ to $\{\boldsymbol{L}'\}$ can be obtained by using the SAS base point vector $\mathbf{b}_i$ as

$$
\mathbf{T} = [\mathbf{x}_i, \mathbf{y}_i, \mathbf{z}_i], \tag{A.18}
$$

where

$$
\mathbf{x}_i = {}^{G}\mathbf{s}_i,
$$

$$
\mathbf{y}_i = {}^{G}\mathbf{s}_i \times \left({}^{G}\mathbf{R}_B \cdot \mathbf{b}_i\right) \Big/ \left\| {}^{G}\mathbf{s}_i \times \left({}^{G}\mathbf{R}_B \cdot \mathbf{b}_i\right) \right\|,
$$

$$
\mathbf{z}_i = \mathbf{x}_i \times \mathbf{y}_i.
$$

In the next section, the Euler's equation for each leg will be derived around the SAS base point B_i. Therefore, linear accelerations of mass centers of the lower and upper parts of the leg will be expressed related to the base point B_i in $\{\boldsymbol{L}'\}$.

As $\mathbf{r}_{Lo}$ and $\mathbf{r}_{Uo}$ denote position vectors of mass centers of the lower and upper parts of the limb in $\{\boldsymbol{L}\}$ and $\{\boldsymbol{U}\}$, position vectors can be transformed to $\{\boldsymbol{L}'\}$ as

$$
\mathbf{r}_{Li} = \mathbf{T}_i \cdot \mathbf{r}_{Lo}, \tag{A.19}
$$

$$
\mathbf{r}_{Ui} = {}^{G}\mathbf{S}_i + \mathbf{T}_i \cdot \mathbf{r}_{Uo}. \tag{A.20}
$$

The linear accelerations of mass centers in $\{\boldsymbol{L}'\}$ can be written as

$$
\mathbf{a}_{Li} = {}^{G}\mathbf{A}_i \times \mathbf{r}_{Li} + {}^{G}\mathbf{W}_i \times \left({}^{G}\mathbf{W}_i \times \mathbf{r}_{Li}\right), \tag{A.21}
$$

$$
\mathbf{a}_{Ui} = {}^{G}\mathbf{A}_i \times \mathbf{r}_{Ui} + {}^{G}\mathbf{W}_i \times \left({}^{G}\mathbf{W}_i \times \mathbf{r}_{Ui}\right) + \ddot{L}_i {}^{G}\mathbf{s}_i + 2\dot{L}_i {}^{G}\mathbf{W}_i \times {}^{G}\mathbf{s}_i. \tag{A.22}
$$

The translational acceleration of the origin of $\{\boldsymbol{L}'\}$ in $\{\boldsymbol{G}\}$ can be obtained as

$$
\mathbf{a}_{Lri} = {}^{G}\ddot{\mathbf{t}}_B + {}^{G}\boldsymbol{\varepsilon}_B \times \left({}^{G}\mathbf{R}_B \cdot \mathbf{b}_i\right) + {}^{G}\boldsymbol{\omega}_B \times \left[{}^{G}\boldsymbol{\omega}_B \times \left({}^{G}\mathbf{R}_B \cdot \mathbf{b}_i\right)\right]. \tag{A.23}
$$

The Euler's equation for the FSS terminal will be derived around the geometrical center o of the end effector. So, the linear acceleration of the mass center of the end effector will be also expressed related to the geometrical center. Similarly, another translational frame $\{\boldsymbol{P}'\}$ is introduced, attached to the geometrical center o and parallel to $\{\boldsymbol{G}\}$.

As $\mathbf{e}_{po}$ is the position vector of the mass center of the FSS terminal (including receivers) in $\{\boldsymbol{P}\}$, the vector can be obtained in $\{\boldsymbol{P}'\}$ as

$$
{}^{G}\mathbf{e}_P = {}^{G}\mathbf{R}_B \cdot {}^{B}\mathbf{R}_P \cdot \mathbf{e}_{Po}. \tag{A.24}
$$

According to the composite theory of rigid body motion, the angular velocity and acceleration of the end effector in $\{\boldsymbol{P}'\}$ can be derived as

$$
{}^{G}\boldsymbol{\varepsilon}_P = {}^{G}\boldsymbol{\varepsilon}_B + {}^{G}\mathbf{R}_B \cdot {}^{B}\boldsymbol{\varepsilon}_P + {}^{G}\boldsymbol{\omega}_B \times \left({}^{G}\mathbf{R}_B \cdot {}^{B}\boldsymbol{\omega}_P\right), \tag{A.25}
$$

$$
{}^{G}\boldsymbol{\omega}_P = {}^{G}\boldsymbol{\omega}_B + {}^{G}\mathbf{R}_B \cdot {}^{B}\boldsymbol{\omega}_P. \tag{A.26}
$$

Then the linear acceleration of the mass center of the end effector under $\{\boldsymbol{P}'\}$ can be written as

$$
\mathbf{a}_P = {}^{G}\boldsymbol{\omega}_P \times \left({}^{G}\boldsymbol{\omega}_P \times {}^{G}\mathbf{e}_P\right) + {}^{G}\boldsymbol{\varepsilon}_P \times {}^{G}\mathbf{e}_P. \tag{A.27}
$$

The linear acceleration of $\{\boldsymbol{P}'\}$ relative to $\{\boldsymbol{G}\}$ can be expressed as

$$
\mathbf{a}_{Pr} = {}^{G}\ddot{\mathbf{t}}_B + {}^{G}\mathbf{R}_B \cdot {}^{B}\ddot{\mathbf{t}}_P + {}^{G}\boldsymbol{\varepsilon}_B \times \left({}^{G}\mathbf{R}_B \cdot {}^{B}\mathbf{t}_P\right) + {}^{G}\boldsymbol{\omega}_B \times \left[{}^{G}\boldsymbol{\omega}_B \times \left({}^{G}\boldsymbol{R}_B \cdot {}^{B}\mathbf{t}_P\right)\right] + 2{}^{G}\boldsymbol{\omega}_B \times \left({}^{G}\mathbf{R}_B \cdot {}^{B}\dot{\mathbf{t}}_P\right). \tag{A.28}
$$

The moment of inertia $\mathbf{I}_{Lo}$ of the upper part of the leg is defined in $\{\boldsymbol{L}\}$, relative to its centroid. The moment of inertia can be obtained in $\{\boldsymbol{L}'\}$ by rotation matrices as

$$
\mathbf{I}_{Li} = \mathbf{T}_i \mathbf{I}_{Lo} \mathbf{T}_i^{\mathrm{T}}. \tag{A.29}
$$

Similarly, $\mathbf{I}_{Uo}$ denotes the moment of inertia of the lower part of the leg in $\{\boldsymbol{U}\}$, relative to its centroid. According to the parallel-axis theorem, the moment of inertia can be obtained in $\{\boldsymbol{L}'\}$ as

$$
\mathbf{I}_{Ui} = \mathbf{T}_i \mathbf{I}_{Uo} \mathbf{T}_i^{\mathrm{T}}. \tag{A.30}
$$

The moment of inertia $\mathbf{I}_{Po}$ of the end effector in $\{\boldsymbol{P}\}$, relative to its centroid, can be transformed to $\{\boldsymbol{P}'\}$ as

$$\mathbf{I}_P = \left({}^G\mathbf{R}_C \cdot {}^C\mathbf{R}_B \cdot {}^B\mathbf{R}_P\right)\mathbf{I}_{Po}\left({}^G\mathbf{R}_C \cdot {}^C\mathbf{R}_B \cdot {}^B\mathbf{R}_P\right)^{\mathrm{T}}. \tag{A.31}$$

So far, all the kinematic parameters required in the dynamic equations of the feed cabin are determined analytically.

Appendix B: Parameters of the FSS

The kinematic and dynamic parameters of the FSS are as follows (default in SI units):

$$\alpha = 30^\circ, \qquad \beta = 15^\circ, \qquad r = 2.5, \qquad R = 5.$$

Base points of the cable-driven Stewart manipulator are:

$$[\mathbf{c}_1\ \mathbf{c}_2\ \mathbf{c}_3\ \mathbf{c}_4\ \mathbf{c}_5\ \mathbf{c}_6] = \begin{bmatrix} 300 & 150 & -150 & -300 & -150 & 150 \\ 0 & 259.8076 & 259.8076 & 0 & -259.8076 & -259.8076 \\ 270 & 270 & 270 & 270 & 270 & 270 \end{bmatrix}.$$

End-effector points of the cable-driven Stewart manipulator are:

$$[\mathbf{d}_1\ \mathbf{d}_2\ \mathbf{d}_3\ \mathbf{d}_4\ \mathbf{d}_5\ \mathbf{d}_6] = \begin{bmatrix} 5.6292 & 0 & 0 & -5.6292 & -5.6292 & 5.6292 \\ -3.25 & 6.5 & 6.5 & -3.25 & -3.25 & -3.25 \\ 0 & 0 & 0 & 0 & 0 & 0 \end{bmatrix}.$$

SAS base points in $\{\boldsymbol{B}\}$ are:

$$[\mathbf{b}_1\ \mathbf{b}_2\ \mathbf{b}_3\ \mathbf{b}_4\ \mathbf{b}_5\ \mathbf{b}_6] = \begin{bmatrix} 2.8284 & 1.0353 & -3.8637 & -3.8637 & 1.0353 & 2.8284 \\ 2.8284 & 3.8637 & 1.0353 & -1.0353 & -3.8637 & -2.8284 \\ 0 & 0 & 0 & 0 & 0 & 0 \end{bmatrix}.$$

SAS end-effector points in $\{\boldsymbol{P}\}$ are:

$$[\mathbf{p}_1\ \mathbf{p}_2\ \mathbf{p}_3\ \mathbf{p}_4\ \mathbf{p}_5\ \mathbf{p}_6] = \begin{bmatrix} 2.4786 & -0.9567 & -1.5219 & -1.5219 & -0.9567 & 2.4786 \\ 0.3263 & 2.3097 & 1.9834 & -1.9834 & -2.3097 & -0.3263 \\ 0.5040 & 0.5040 & 0.5040 & 0.5040 & 0.5040 & 0.5040 \end{bmatrix}.$$

Mass center of lower part of each leg in $\{\boldsymbol{U}\}$ is:

$$\mathbf{r}_{Uo} = [1.9909\ 0\ 0]^{\mathrm{T}}.$$

Mass center of upper part of each leg in $\{\boldsymbol{L}\}$ is:

$$\mathbf{r}_{Lo} = [-1\ 0\ 0]^{\mathrm{T}}.$$

Mass center of the SAS base in $\{\boldsymbol{B}\}$ is:

$$\mathbf{e}_B = [-0.04748\ 0.00033\ 0.082894]^{\mathrm{T}}.$$

Mass center of the framework in $\{\boldsymbol{L}_S\}$ is:

$$\mathbf{e}_f = [0.19136\ 0\ 0.42644]^{\mathrm{T}}.$$

Position vector of the centroid of the SAS base in $\{\boldsymbol{M}\}$ is:

$$\mathbf{t}_B = [0\ 0\ 1.25]^{\mathrm{T}}.$$

Position of the origin of $\{\boldsymbol{L}_S\}$ in $\{\boldsymbol{L}_f\}$ is:

$$\mathbf{t}_f = [0\ 0\ -1.58457]^{\mathrm{T}}.$$

Position of the intersection of two revolution axes of the A–B rotator in $\{\boldsymbol{C}\}$ is:

$${}^{C}\mathbf{t}_M = [0\ 0\ -5.6]^{\mathrm{T}}.$$

Mass of lower and upper parts of each leg is:

$$m_L = 461.16613 \quad \text{and} \quad m_U = 44.10796.$$

Moment of inertia of lower part of each leg in $\{\boldsymbol{U}\}$ is:

$$\mathbf{I}_{Uo} = \begin{bmatrix} 1.83 \times 10^3 & & \\ & 0.67 \times 10^3 & \\ & & 0.67 \times 10^3 \end{bmatrix}.$$

Moment of inertia of upper part of each leg in $\{\boldsymbol{L}\}$ is:

$$\mathbf{I}_{Lo} = \begin{bmatrix} 44.20 & & \\ & 58.86 & \\ & & 58.86 \end{bmatrix}.$$

Mass of the SAS end effector is:

$$m_P = 3698.04273.$$

Mass of the SAS base is:

$$m_B = 5929.84427.$$

Mass of the cable platform is:

$$m_C = 15687.42379.$$

Mass of the framework is:

$$m_F = 7901.29622.$$

Gravity vector is:

$$\mathbf{g} = [0\ 0\ -9.80664]^{\mathrm{T}}.$$

Mass center of the end effector in $\{\boldsymbol{P}\}$ is:

$$\mathbf{e}_o = [-0.04369\ -0.02018\ -0.25225]^{\mathrm{T}},$$

Moment of inertia of the end effector in $\{\boldsymbol{P}\}$ is:

$$\mathbf{I}_{Po} = \begin{bmatrix} 7.86 \times 10^3 & -1.21 \times 10^2 & -12.13 \\ -1.21 \times 10^2 & 7.76 \times 10^3 & -18.88 \\ -12.13 & -18.88 & 1.412 \times 10^4 \end{bmatrix}.$$

Moment of inertia of the framework in $\{\boldsymbol{L}_S\}$ is:

$$\mathbf{I}_{fo} = \begin{bmatrix} 1.1256 \times 10^5 & 1.476 \times 10^2 & -2.419 \times 10^3 \\ 1.476 \times 10^2 & 1.2034 \times 10^5 & -2.6215 \times 10^2 \\ -2.419 \times 10^3 & -2.6215 \times 10^2 & 2.0123 \times 10^5 \end{bmatrix}.$$

Moment of inertia of the SAS base in $\{\boldsymbol{B}\}$ is:

$$\mathbf{I}_{Bo} = \begin{bmatrix} 3.9620 \times 10^4 & 0 & -4.2186 \times 10^2 \\ 0 & 7.1376 \times 10^4 & 0 \\ -4.2186 \times 10^2 & 0 & 8.6972 \times 10^4 \end{bmatrix}.$$

References

1. Nan, R., Peng, B.: A Chinese concept for the 1 km^2 radio telescope. Acta Astronaut. **46**(10–12), 667–675 (2000)
2. Nan, R.: Five hundred meter aperture spherical radio telescope (FAST). Sci. China Ser. G, Phys. Mech. Astron. **49**(2), 129–148 (2006)
3. Sharon, A.: The macro/micro manipulator: an improved architecture for robot control. Ph.D. Thesis, Massachusetts Institute of Technology (1988)
4. Cheng, Y., Ren, G., Dai, S.L.: The multi-body system modeling of the Gough–Stewart platform for vibration control. J. Sound Vib. **27**(3), 599–614 (2004)

5. Yao, R., Tang, X., Wang, J., Huang, P.: Dimension optimization design of the four-cable driven parallel manipulator in FAST. IEEE/ASME Trans. Mechatron. **15**(6), 932–941 (2010)
6. Do, W.Q.D., Yang, D.C.H.: Inverse dynamic analysis and simulation of a platform type of robot. J. Intell. Robot. Syst. **5**(3), 209–227 (1988)
7. Ji, Z.: Study of the effect of leg inertia in Stewart platforms. In: Proceedings of the 1993 IEEE International Conference on Robotics and Automation, Atlanta, GA, May 2–4, pp. 121–126 (1993)
8. Dasgupta, B., Mruthyunjaya, T.S.: Closed-from dynamic equations of the general Stewart platform through the Newton–Euler approach. Mech. Mach. Theory **33**(7), 993–1012 (1998)
9. Dasgupta, B., Mruthyunjaya, T.S.: Dynamic stability index and vibration analysis of a flexible Stewart platform. J. Sound Vib. **307**(3–5), 579–587 (2007)
10. Li, Y., Xu, Q.: Kinematics and inverse dynamics analysis for a general 3-PRS spatial parallel mechanism. Robotica **23**(2), 219–229 (2005)
11. Wang, J., Gosselin, C.M.: A new approach for the dynamic analysis of parallel manipulators. Multibody Syst. Dyn. **2**(3), 317–334 (1998)
12. Abdellatif, H., Heimann, B.: Computational efficient inverse dynamics of 6-DOF fully parallel manipulators by using the Lagrangian formalism. Mech. Mach. Theory **44**(1), 192–207 (2009)
13. Staicu, S., Liu, X.-J., Wang, J.: Inverse dynamics of the HALF parallel manipulator with revolute actuators. Nonlinear Dyn. **50**(1–2), 1–12 (2007)
14. Staicu, S., Liu, X.-J., Li, J.: Explicit dynamics equations of the constrained robotic systems. Nonlinear Dyn. **58**(1–2), 217–235 (2009)
15. Shao, Z., Tang, X., Chen, X., Wang, L.: Inertia match research of a 3-RRR reconfigurable planar parallel manipulator. Chin. J. Mech. Eng. **22**(6), 791–799 (2009)
16. Staicu, S., Zhang, D.: A novel dynamic modelling approach for parallel mechanisms analysis. Robot. Comput.-Integr. Manuf. **24**(1), 167–172 (2008)
17. Koekebakker, S.: Model based control of a flight simulator motion system. Ph.D. Thesis, Delft University of Technology (2001)
18. Yuan, Y., Li, Y.: Multi-degree of freedom vibration model for a 3-DOF hybrid robot. In: Proceedings of 2009 IEEE/ASME International Conference on Advanced Intelligent Mechatronics, Singapore, July 14–17, pp. 1467–1472 (2009)
19. van Oosterhout, G.P.C.: The wind-induced dynamic response of tall buildings: a comparative study. J. Wind Eng. **64**(2–3), 135–144 (1999)